



Surface heat assessment for developed environments: Probabilistic urban temperature modeling



Carl Malings^{a,*}, Matteo Pozzi^b, Kelly Klima^c, Mario Bergés^b, Elie Bou-Zeid^d, Prathap Ramamurthy^e

^a Department of Civil and Environmental Engineering, CMU, 5000 Forbes Avenue, Pittsburgh, PA 15213, United States

^b Department of Civil and Environmental Engineering, Faculty Affiliate – Scott Institute for Energy Innovation, CMU, 5000 Forbes Avenue, Pittsburgh, PA 15213, United States

^c Research Engineer, Engineering and Applied Sciences, RAND Corporation, 1776 Main Street, m3105, Santa Monica, CA 90401, United States

^d Department of Civil and Environmental Engineering, Princeton University, 59 Olden Street, Princeton, NJ 08544, United States

^e Department of Mechanical Engineering, City College of New York, 160 Convent Avenue, New York, NY 10031, United States

ARTICLE INFO

Article history:

Received 5 February 2017

Received in revised form 10 July 2017

Accepted 30 July 2017

Available online xxxx

ABSTRACT

Extreme heat waves, exacerbated by the urban heat island effect, have major impacts on the lives and health of city residents. Projected future temperature increases for many urban areas of the United States will further exacerbate these impacts. Accurate predictions of the spatial and temporal distribution of risk associated with such heat waves can support the optimal implementation of strategies to mitigate these risks, such as the issuance of heat advisories and the activation of cooling centers. In this paper, we describe how fine resolution simulations of historic extreme heat events are generated and used to train a probabilistic spatio-temporal model of the temperature distribution in an urban area. We further demonstrate how this model can be used to combine temperature data from various sources and downscale regional predictions in order to provide accurate fine resolution temperature forecasts. Applications of this model are presented for two urban areas: New York City, NY and Pittsburgh, PA, USA. Based on simulated temperature data from fine resolution forecasting models, we find that this probabilistic method can improve the prediction accuracies of urban temperatures, locally and especially in the short-term, with respect to other temperature forecasting and interpolation methods, such as the use of average city-wide temperature predictions and estimates at discrete weather stations.

© 2017 Published by Elsevier Ltd.

1. Introduction

Recent extreme heat waves across North America, Europe, and Australia (Andrews, 1994; Berko, Ingram, Saha, & Parker, 2014; Davis, Knappenberg, Michaels, & Novicoff, 2003; Geerts & Linacre, 1999; Kalkstein & Greene, 1997; Robine et al., 2008) have demonstrated the adverse health impacts which high temperatures can have. Land surface temperature is one of the most important factors related to the impacts of extreme heat (Mushore, Mutanga, Odindi, & Dube, 2017). Even a 1 °C difference in surface temperatures can result in a 4.5% increase in heat mortality risk (Anderson & Bell, 2011). Furthermore, in what is known as the urban heat island (UHI) effect, human activities and land use changes in developed areas lead to urban air temperatures being on average 1 to 3 °C warmer than their rural surroundings during daytime (Oke, 1997; Sailor, 2002; US EPA, 2012), and up to 12 °C warmer at night (Oke, 1997). Worse still, the UHI effect interacts synergistically with heat waves to produce extreme heat stresses in urban areas that exceed the simple sum of the two effects (Li & Bou-Zeid, 2013). Extreme

temperatures therefore represent a major risk to urban dwellers, especially considering that future heat waves are predicted to be more intense and frequent (e.g., a 2 to 5 °C increase in average near-surface air temperatures at 2m above ground level is expected in the Northeast U.S. by 2100 (Melillo, Richmond, & Yohe, 2014)). Globally, intensifying urbanization is increasing the extent and magnitude of the UHI in many major population centers, such as Dhaka, Bangladesh (Dewan & Corner, 2014) and the Pearl River Delta in China (Chen, Zhao, Li, & Yin, 2006; Li, Cao, Lang, & Wu, 2017). Due to these increasing risks, many cities are beginning to focus their attention on adaptation, hazard mitigation, and emergency response plans for high temperatures (NYCPCC, 2013; Menne & Matthies, 2009; Parson & Jameson, 2012; Rhoades, Contreras, Garrett, Bakshi, & Bellomo, 2014; Sustainable, 2013). Urban planners can more appropriately respond to current and future temperature risks by improving their understanding of the effects of land use changes and mitigation strategies (e.g., cool or green roofs) on the UHI (Dewan & Yamaguchi, 2009; Li, Bou-Zeid, & Oppenheimer, 2014; Trotter, Dewan, & Robinson, 2017).

To understand and forecast risks associated with extreme heat, physical models of urban microclimates have been developed. One such model is the Princeton Urban Canopy Model (PUCM) (Wang, Bou-Zeid, & Smith, 2013), developed as an extension of the National

* Corresponding author.

E-mail addresses: cmalings@andrew.cmu.edu (C. Malings), mpozzi@cmu.edu (M. Pozzi).

Table 1
WRF-PUCM simulation settings.

Setting		Value (New York)	Value (Pittsburgh)
Simulation area	[km]	159 × 159	198 × 201
Spatial grid spacing	[km]	1	1
Calibration period start date		July 15, 2006	June 15, 2012
Calibration period end date		July 21, 2006	June 21, 2012
Calibration period duration	[days]	7	7
Calibration period temporal grid spacing	[hr]	1	0.5
validation period start date		July 22, 2006	June 22, 2012
Validation period end date		August 9, 2006	July 13, 2012
Validation period duration	[days]	19	22
Validation period temporal grid spacing	[hr]	0.5	0.5

Center for Atmospheric Research's WRF-ARW (Weather Research and Forecasting – Advanced Research WRF) model (Skamarock et al., 2005). The PUCM extension incorporates fine resolution representations of urban surface heterogeneity and hydrology, significantly improving urban temperature forecasting over WRF's default urban canopy model (Li & Bou-Zeid, 2014). However, such deterministic models are computationally intensive, making them difficult to use for short-term predictions of urban temperatures. For such predictions, they must be re-run as updated global meteorological information is obtained. Furthermore, to reflect a range of uncertainty, they must be re-run for a variety of initial conditions and model setups to generate an ensemble forecast (Lin-Jiong, Yi-Min, Qing, Hai-Yang, & Guo-Xiong, 2012; Sper de Almeida & Bauer, 2012; Worley et al., 2011).

While deterministic models can express uncertainty implicitly through variation of the model inputs among multiple runs, probabilistic modeling explicitly represents uncertainty in predictions. This is done by adopting appropriate structures on correlation and interdependence of the outputs. Probabilistic modeling for spatially and temporally distributed fields, such as temperature, is known as *geostatistics* (Cressie & Wikle, 2011). One class of widely used geostatistical models is the Gaussian process (Rasmussen & Williams, 2006). These models extend the multivariate Gaussian distribution to a continuous domain using mean and covariance functions. Gaussian processes and random fields have been used for a variety of applications, including modeling spatially distributed rainfall intensity, corrosion initiation, and seismic risk (Krause, Singh, & Guestrin, 2008; Malings & Pozzi, 2014; Straub, 2011). Statistical inference from data using Gaussian process models is

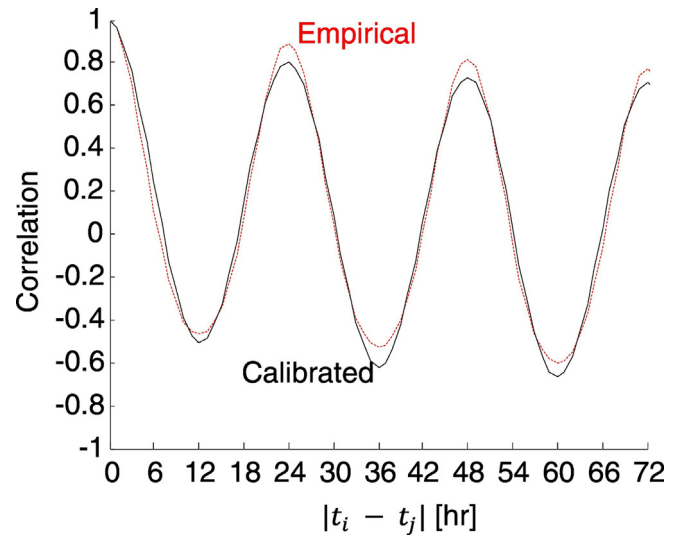


Fig. 2. Comparison between the empirically observed temporal correlation of $T_0(t)$, as computed from simulated temperature data for New York City (dotted line), and the calibrated covariance function of Eq. (11) (solid line).

also relatively efficient (Cressie & Wikle, 2011; Rasmussen & Williams, 2006).

In this paper, we investigate how well a Gaussian process model can predict urban temperature patterns by comparing the predictions of a calibrated model against those of a fine resolution deterministic dynamical urban micro-climate model. The motivation for the development of this model is to provide a computationally efficient probabilistic method, which can serve as a surrogate to more intensive deterministic simulations for urban temperature prediction. We demonstrate the proposed method in two case studies: New York City, NY and Pittsburgh, PA, USA.

2. Probabilistic urban temperature modeling

In this paper, we decompose the temperature field into three components and describe each using a Gaussian process random field model. Section 2.1 provides a description of the temperature decomposition used in this paper. Section 2.2 gives an overview of the Gaussian

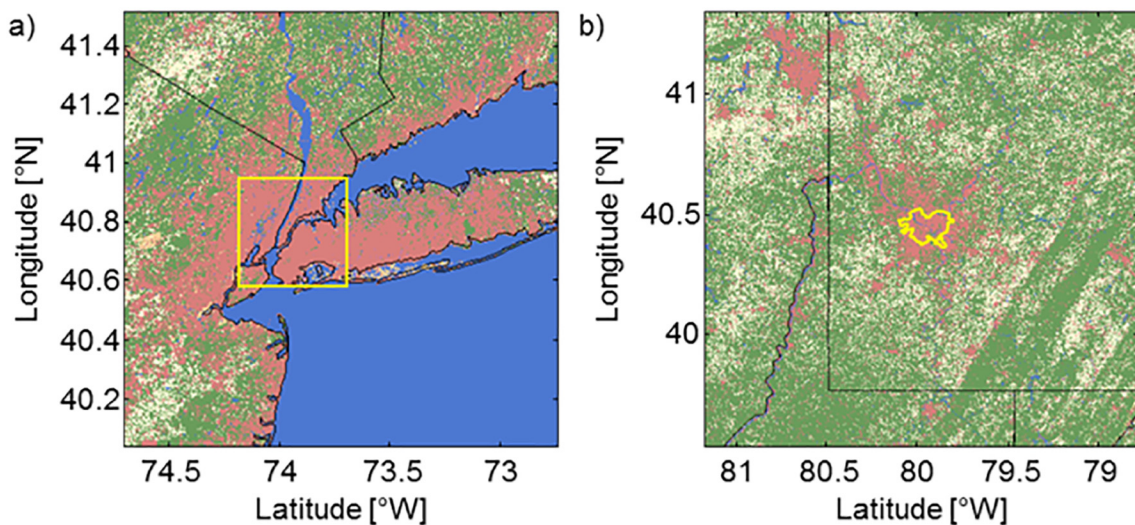


Fig. 1. Land use within the simulation regions for New York City (a) and Pittsburgh (b); land use maps from the National Land Cover Database (Homer et al., 2015). Red color indicates urban areas, green and tan indicate rural areas, and blue indicates water; full map and legend available at https://gis1.usgs.gov/csas/gap/viewer/land_cover/Map.aspx. Yellow outlines indicate the reduced domains used for validation in Section 4. (For interpretation of the references to color in this figure legend, the reader is referred to the web version of this article.)

Table 2Calibrated hyperparameters of the covariance function for $T_0(t)$.

Hyperparameter		Value (New York)	Value (Pittsburgh)
μ_{T_0}	[°C]	31.5	24.5
σ_{T_0}	[°C]	5.97	6.66
α_{T_0}	[–]	0.31	0.34
λ_{T_0}	[hr]	23.7	23.3

process modeling framework, and Sections 2.3, 2.4, and 2.5 discuss the specific models developed for the elements of the decomposed temperature. In Section 2.6, we combine these models into the overall Gaussian process temperature model. Appendix A provides a table of all variables used and their definitions.

2.1. Temperature decomposition

Given a location \mathbf{x} and a time t , let the spatio-temporal field of surface temperature over a specified domain (in degrees Celsius) be denoted by $T(\mathbf{x}, t)$. We decompose this temperature field as:

$$T(\mathbf{x}, t) = T_0(t) + T'(\mathbf{x}, t) \quad (1)$$

where $T_0(t)$ is the mean surface temperature over the domain (i.e. over all \mathbf{x} , for each time t) and $T'(\mathbf{x}, t)$ is the perturbation from this value (i.e., the expected value of this perturbation over \mathbf{x} is zero at each time t). Given this formulation, $T_0(t)$ can be interpreted as e.g. the average city-wide temperature as a function of time.

We further decompose the perturbation as:

$$T'(\mathbf{x}, t) = T_1(\mathbf{x}, t) + T''(\mathbf{x}, t) \quad (2)$$

where $T_1(\mathbf{x}, t)$ is the spatially and temporally varying temperature pattern at location \mathbf{x} and at time t . We define this pattern to be cyclic, recurring at a fixed time interval $\Delta t = 24$ h, capturing a daily cycle. Depending on the application, additional terms may be added to include other cyclic temperature patterns, e.g. seasonal patterns. In the context of urban temperature, $T_1(\mathbf{x}, t)$ captures the UHI effect as it varies across space and throughout the day. Finally, $T''(\mathbf{x}, t)$ is the temperature residual, which captures the variability in the temperature that is not described by either $T_0(t)$ or $T_1(\mathbf{x}, t)$. The origins of $T''(\mathbf{x}, t)$ are stochastic and can be traced to various physical processes such as non-cyclic anthropogenic heat emissions or the influence of wind patterns and clouds on surface temperatures.

Combining Eqs. (1) and (2) above yields the full temperature decomposition:

$$T(\mathbf{x}, t) = T_0(t) + T_1(\mathbf{x}, t) + T''(\mathbf{x}, t) \quad (3)$$

2.2. Gaussian process models

Gaussian process models extend the multivariate Gaussian distribution to a continuous spatial and/or temporal domain over which variables are defined (Rasmussen & Williams, 2006). A Gaussian process model describes the value of any field F at spatial location \mathbf{x} and temporal coordinate t as a Gaussian variable with mean and variance defined by using the mean and covariance functions of the model. This model is denoted:

$$f(\mathbf{x}, t) \sim \mathcal{GP}(M(\mathbf{x}, t), K(\mathbf{x}_i, t_i, \mathbf{x}_j, t_j)) \quad (4)$$

where $M(\mathbf{x}, t)$ is the mean function and $K(\mathbf{x}_i, t_i, \mathbf{x}_j, t_j)$ is the covariance function. For any finite set of n_x locations $X = \{\mathbf{x}_1, \dots, \mathbf{x}_{n_x}\}$ and n_t timesteps $\tau = \{t_1, \dots, t_{n_t}\}$, the Gaussian process defines a prior multivariate Gaussian distribution for \mathbf{f} , the vector of random values of the field at each pair of these spatial and temporal coordinates:

$$\mathbf{f} \sim \mathcal{N}(\boldsymbol{\mu}_F, \mathbf{K}_F) \quad (5)$$

where \mathcal{N} denotes the Gaussian distribution function, $\boldsymbol{\mu}_F$ is the mean vector, obtained by evaluating $M(\mathbf{x}, t)$ at each pair of space and time coordinates, and \mathbf{K}_F is the covariance matrix, obtained by evaluating $K(\mathbf{x}_i, t_i, \mathbf{x}_j, t_j)$ at all pairs of space-time coordinates.

Gaussian processes also allow for efficient probabilistic inference for updating predictions based on data. Let Y be a set of measurements of random field F , with the vector of values of these measurements denoted \mathbf{y} . We assume that \mathbf{y} is a measurement of one or more linear combinations of elements in \mathbf{f} with zero-mean Gaussian noise:

$$\mathbf{y} = \boldsymbol{\beta}_Y \mathbf{f} + \boldsymbol{\epsilon} \quad \boldsymbol{\epsilon} \sim \mathcal{N}(\mathbf{0}, \mathbf{K}_\epsilon) \quad (6)$$

where $\boldsymbol{\beta}_Y$ is a matrix specifying the elements or combinations of elements in \mathbf{f} which are observed. The matrix \mathbf{K}_ϵ indicates the covariance of the measurement noise. Often, including for the applications presented in this paper, independence between measurement errors is assumed, resulting in a diagonal matrix. However, alternative specific correlation structures for the errors can also be modeled through appropriate definition of this matrix.

As linear combinations of Gaussian random variables, these measures are themselves Gaussian:

$$\mathbf{y} \sim \mathcal{N}(\boldsymbol{\mu}_Y, \mathbf{K}_Y) \quad \boldsymbol{\mu}_Y = \boldsymbol{\beta}_Y \boldsymbol{\mu}_F \quad \mathbf{K}_Y = \boldsymbol{\beta}_Y \mathbf{K}_F \boldsymbol{\beta}_Y^T + \mathbf{K}_\epsilon \quad (7)$$

Conditional to these measurements of the field, the prior distribution of the field in Eq. (5) is updated to a posterior distribution:

$$\mathbf{f} | \mathbf{y} \sim \mathcal{N}(\boldsymbol{\mu}_{F|Y}, \mathbf{K}_{F|Y}) \quad (8)$$

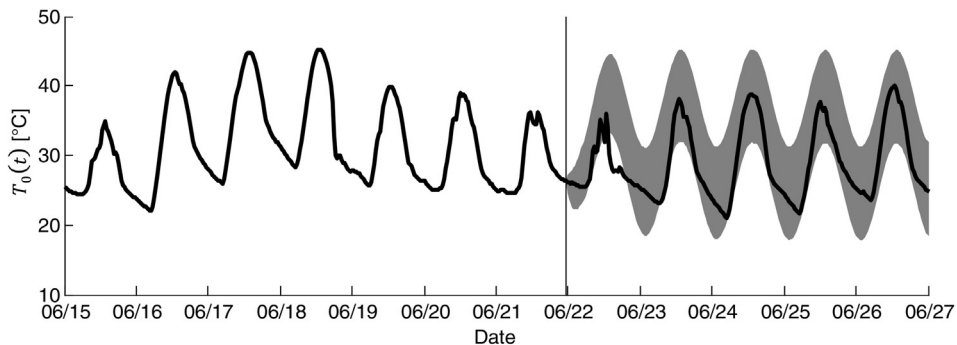


Fig. 3. Temperature predictions using a Gaussian process model for $T_0(t)$. The average temperature before 6/22 is used as training data, and the resulting 95% confidence bounds on the predictions of future temperatures are shown as the grey area, along with the actual temperature record (black line).

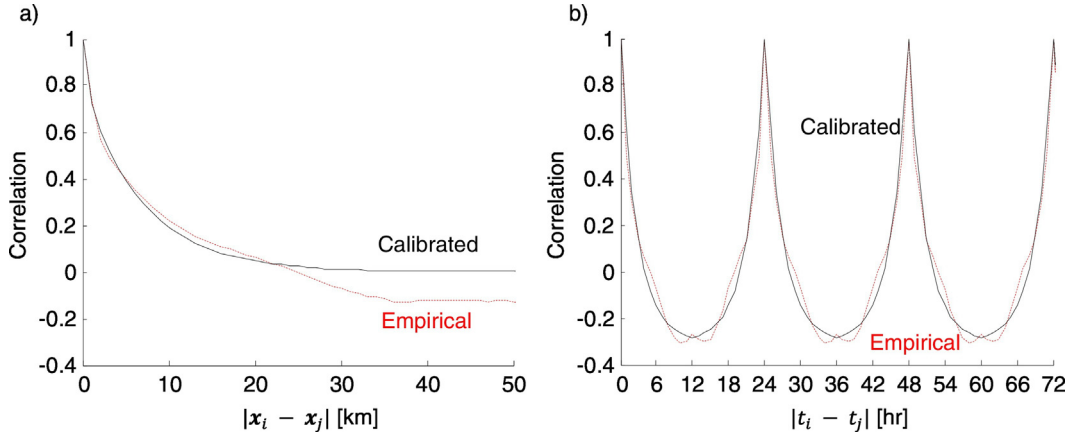


Fig. 4. Comparison between the empirically observed spatial (a) and temporal (b) correlations of $T_1(\mathbf{x}, t)$, as computed from simulated temperatures for New York City (dotted line), and the calibrated covariance functions of Eqs. (15) and (16) (solid line).

The posterior mean and covariance of the field are computed as follows:

$$\boldsymbol{\mu}_{F|Y} = \boldsymbol{\mu}_F + \mathbf{K}_{FY}\mathbf{K}_Y^{-1}(\mathbf{y} - \boldsymbol{\mu}_Y) \quad \mathbf{K}_{F|Y} = \mathbf{K}_F - \mathbf{K}_{FY}\mathbf{K}_Y^{-1}\mathbf{K}_{FY}^T \quad (9)$$

where $\mathbf{K}_{FY} = \mathbf{K}_F\boldsymbol{\beta}_Y^T$. Rasmussen & Williams (Rasmussen & Williams, 2006) provide a definitive text describing Gaussian processes and their applications, including derivations for the above equations.

2.3. Global mean temperature

We model the global mean of the temperature $T_0(t)$ for the region at time t as:

$$T_0(t) \sim \mathcal{GP}(\boldsymbol{\mu}_{T_0}, K_{T_0}(t_i, t_j)) \quad (10)$$

where $\boldsymbol{\mu}_{T_0}$ denotes the expected mean temperature in the region over time and $\mathbf{K}_{T_0}(t_i, t_j)$ models the temporal covariance in these temperatures. We estimate the average $\boldsymbol{\mu}_{T_0}$ from summertime temperature records for the period simulated by the WRF-PUCM model as training data for a region (as discussed in Section 3.2). This value will in fact vary seasonally and over longer time horizons due to climate change. However, as this model is used (in the current work) for predictions over periods of several hours, variation in this term is assumed to be negligible.

We use a covariance function with a combined exponential and periodic correlation structure to model the daily cyclic variations in global temperatures. This function is:

$$K_{T_0}(t_i, t_j) = \sigma_{T_0}^2 \left(\alpha_{T_0} \exp\left(-\frac{|t_i - t_j|}{\lambda_{T_0}}\right) + (1 - \alpha_{T_0}) \cos\left(2\pi \frac{|t_i - t_j|}{\Delta t}\right) \right) \quad (11)$$

This function models the decay in correlation between the average temperatures at two times (t_i and t_j) as the absolute difference between these times, $|t_i - t_j|$, increases. It also models periodic correlation, capturing the day/night temperature cycle. The hyperparameter (i.e. parameter of the covariance function) λ_{T_0} is the correlation timescale, σ_{T_0} is the marginal standard deviation of the average temperature, and α_{T_0} is a weighting coefficient (i.e. if $\alpha_{T_0} = 1$, the correlation is purely exponential, while if $\alpha_{T_0} = 0$ it is purely periodic). The calibration of hyperparameters is described in Section 3.2.

In this paper, regional forecasts of the average temperature, e.g. forecasts by the National Weather Service (NWS) made using coarse

resolution WRF models, are processed as pseudo-observations of the global mean temperature. These observations are modeled as:

$$Y_{T_0}(t) = \frac{1}{n_X} \sum_{\mathbf{x} \in X} T(\mathbf{x}, t) + \epsilon_{T_0}(t) \quad (12)$$

Errors in these measurements are denoted $\epsilon_{T_0}(t)$; we assume here that this error is negligible, i.e. $\epsilon_{T_0}(t) = 0 \forall t \in \tau$, since the average temperatures used for this model are computed from simulated temperature data (as discussed in Section 3.1). More sophisticated error models might be used where simulation domain definitions and/or spatial resolutions differ between the models used for model calibration and for temperature prediction.

We process these observations as outlined in Section 2.2 to update the prior global mean model of Eq. (10) to a posterior model. We then use models of the cyclic temperature patterns and residuals to perform statistical downscaling from these coarse resolution predictions to improve fine resolution forecasting, as discussed below.

2.4. Cyclic temperature pattern

The cyclic temperature pattern captures the systematic differences in temperature between parts of a region and the global average temperature throughout the day. We model this pattern as a Gaussian process:

$$T_1(\mathbf{x}, t) \sim \mathcal{GP}(\mathbf{0}, \mathbf{K}_{T_1}(\mathbf{x}_i, t_i, \mathbf{x}_j, t_j)) \quad (13)$$

The prior expected value of this pattern in space and time is zero; areas that are systematically above or below the average temperature due to the UHI will be identified in the posterior model conditional to training data.

Table 3

Calibrated hyperparameters of the covariance function for $T_1(\mathbf{x}, t)$.

Hyperparameter		Value (New York)	Value (Pittsburgh)
σ_{T_1}	[°C]	0.44	0.58
$\alpha_{T_1, X}$	[—]	0.8	0.7
$\lambda_{T_1, X, 1}$	[km]	7.0	7.9
$\lambda_{T_1, X, 2}$	[km]	0.5	7.8
$\alpha_{T_1, \tau}$	[—]	−0.3	−1.5
$\lambda_{T_1, \tau}$	[hr]	2.8	10.3

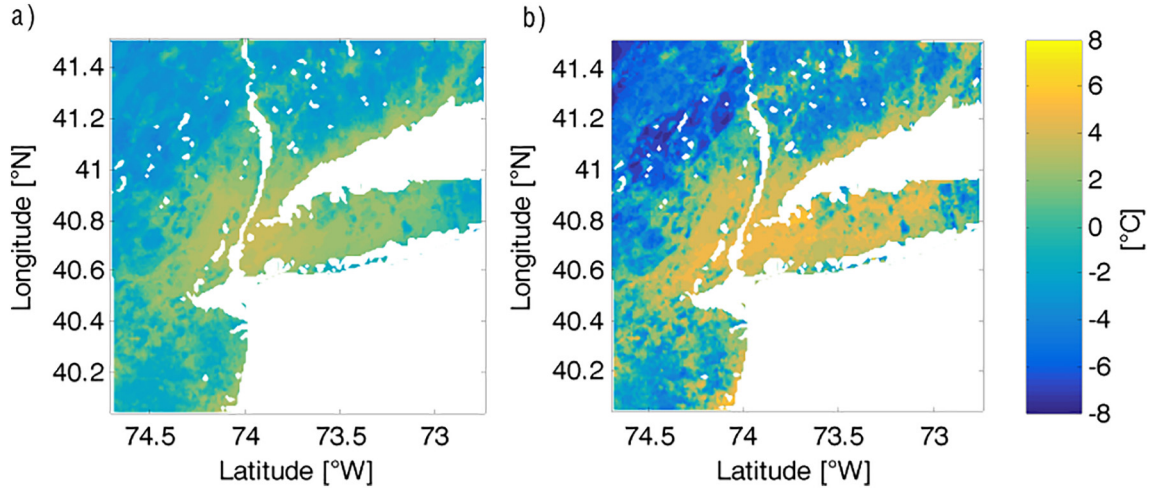


Fig. 5. Posterior mean of the spatial temperature patterns $T_1(\mathbf{x}, t)$ for New York City at local midnight (a) and noon (b), conditioned on measurements of these patterns, as in Eq. (18), obtained from the training data set.

We assume that the covariance function is separable as:

$$K_{T_1}(\mathbf{x}_i, t_i, \mathbf{x}_j, t_j) = \sigma_{T_1}^2 K_{T_1, X}(\mathbf{x}_i, \mathbf{x}_j) K_{T_1, \tau}(t_i, t_j) \quad (14)$$

The hyperparameter $\sigma_{T_1}^2$ describes the variance of the cyclic pattern. The spatial covariance is:

$$K_{T_1, X}(\mathbf{x}_i, \mathbf{x}_j) = \alpha_{T_1, X} \exp\left(-\frac{|\mathbf{x}_i - \mathbf{x}_j|}{\lambda_{T_1, X, 1}}\right) + (1 - \alpha_{T_1, X}) \exp\left(-\frac{|\mathbf{x}_i - \mathbf{x}_j|}{\lambda_{T_1, X, 2}}\right) \quad (15)$$

This represents the weighted average (with coefficient $\alpha_{T_1, X}$) of two exponential correlation functions with length parameters $\lambda_{T_1, X, 1}$ and $\lambda_{T_1, X, 2}$, where $|\mathbf{x}_i - \mathbf{x}_j|$ denotes the Euclidian distance between \mathbf{x}_i and \mathbf{x}_j . This mixture format was found to best capture the empirical correlation structure with the fewest number of parameters, as described in Section 3.3.

The temporal covariance is:

$$K_{T_1, \tau}(t_i, t_j) = (1 - \alpha_{T_1, \tau}) \exp\left(-\frac{|t_i - t_j|_{\text{cyl}}}{\lambda_{T_1, \tau}}\right) + \alpha_{T_1, \tau} \quad (16)$$

where $|t_i - t_j|_{\text{cyl}}$ denotes the daily cyclic time duration between t_i and t_j :

$$|t_i - t_j|_{\text{cyl}} = \min(|t_i - t_j| \bmod \Delta t, \Delta t - |t_i - t_j| \bmod \Delta t) \quad (17)$$

This reflects an exponential correlation applied to a transformation of the temporal domain to give the covariance a cyclic property. The use of this cyclic exponential model, rather than a sinusoidal model as in Eq. (11), better matches the empirical correlation structure of the cyclic temperature patterns, as discussed in Section 3.3.

Fine resolution data from historical events provides pseudo-observations for updating this prior model. Such observations are of the form:

$$Y_{T_1}(\mathbf{x}, t_{\text{cyl}}) = \frac{1}{n_{\text{cyl}}} \sum_{t \in \tau_{\text{cyl}}} [T(\mathbf{x}, t) - Y_{T_0}(t)] + \epsilon_{T_1}(\mathbf{x}, t_{\text{cyl}}) \quad (18)$$

where $\tau_{\text{cyl}} = \{t_1, \dots, t_{n_{\text{cyl}}}\}$ is the set of n_{cyl} time steps in the data set at the same time of day, such that:

$$t \bmod \Delta t = t_{\text{cyl}} \quad \forall t \in \tau_{\text{cyl}} \quad (19)$$

That is, pseudo-observations represent the average difference between the temperature field and the global average temperature at a certain time during the diurnal cycle. The error in these measurements is assumed to be negligible, i.e. $\epsilon_{T_1}(\mathbf{x}, t_{\text{cyl}}) = 0 \forall \mathbf{x} \in X, t_{\text{cyl}} \in \tau_{\text{cyl}}$. By conditioning this cyclic pattern on these observations, information about land characteristics and their effect on the spatial distribution of temperature

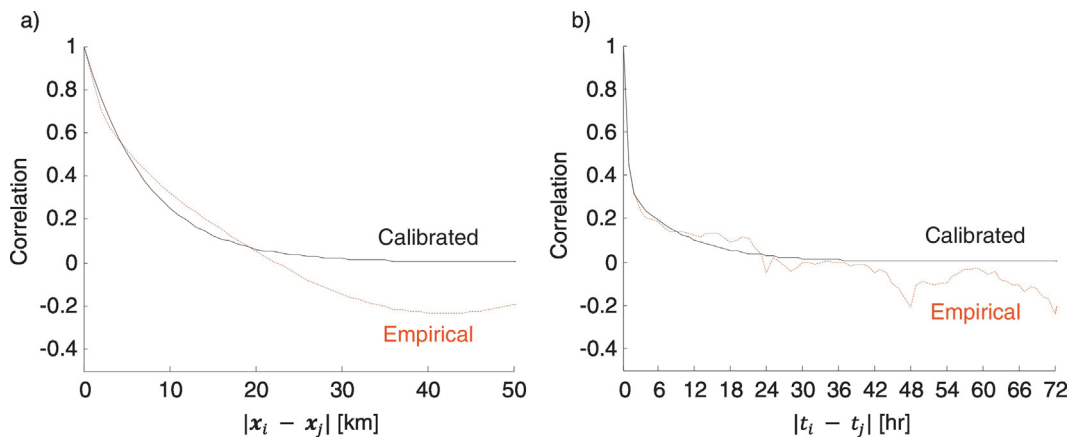


Fig. 6. Comparisons between the empirical spatial (a) and temporal (b) correlations in the residual temperature fields for New York City, NY (dotted line), compared to the trained covariance functions (solid line).

Table 4
Calibrated hyperparameters of the covariance function for $T^*(\mathbf{x}, t)$.

Hyperparameter		Value (New York)	Value (Pittsburgh)
$\lambda_{T^*, X}$	[km]	7.25	7.16
$\alpha_{T^*, \tau}$	[—]	0.64	0.55
$\lambda_{T^*, \tau, 1}$	[hr]	0.6	0.45
$\lambda_{T^*, \tau, 2}$	[hr]	9.5	4.1

is captured by the posterior model. Finally, note that changes in land cover alter the UHI pattern, so new fine resolution simulations are required to generate pseudo-observation data to capture such changes (Li et al., 2014).

2.5. Residual temperature

The residual temperature field captures all temperature phenomena not included in the models above. While the influence of factors such as soil moisture and cloud cover are modeled deterministically by WRF-PUCM at high computational cost, these influences are treated here as sources of randomness captured in the residual temperature and modeled by a Gaussian process:

$$T^*(\mathbf{x}, t) \sim \mathcal{GP}(\mathbf{0}, K_{T^*}(\mathbf{x}_i, t_i, \mathbf{x}_j, t_j)) \quad (20)$$

We assume the covariance is separable:

$$K_{T^*}(\mathbf{x}_i, t_i, \mathbf{x}_j, t_j) = \sigma_{T^*}(\mathbf{x}_i) \sigma_{T^*}(\mathbf{x}_j) K_{T^*, X}(\mathbf{x}_i, \mathbf{x}_j) K_{T^*, \tau}(t_i, t_j) \quad (21)$$

where $\sigma_{T^*}(\mathbf{x})$ denotes the standard deviation of the residual field at \mathbf{x} . The spatial covariance is exponential:

$$K_{T^*, X}(\mathbf{x}_i, \mathbf{x}_j) = \exp\left(-\frac{|\mathbf{x}_i - \mathbf{x}_j|}{\lambda_{T^*, X}}\right) \quad (22)$$

The temporal covariance function is the weighted average of two exponential functions:

$$K_{T^*, \tau}(t_i, t_j) = \alpha_{T^*, \tau} \exp\left(-\frac{|t_i - t_j|}{\lambda_{T^*, \tau, 1}}\right) + (1 - \alpha_{T^*, \tau}) \exp\left(-\frac{|t_i - t_j|}{\lambda_{T^*, \tau, 2}}\right) \quad (23)$$

This mixture model best captures the empirical correlation of the residual temperature field, as discussed in Section 3.4.

Table 5
Test cases for model validation.

Case	$Y_{T_0}(t)$ (accurate forecast)	$Y_{T_1}(\mathbf{x}, t)$ (fine resolution training data)	$Y_{T^*}(\mathbf{x}, t)$ (local measurements)
1			✓
2	✓		✓
3	✓	✓	
4	✓	✓	✓
BL-1	✓		
BL-2			✓

2.6. Gaussian process temperature model

Because the sum of Gaussian random variables is itself described by a Gaussian distribution, we combine the separate models developed above into an overall Gaussian process urban temperature model, assuming independence between these models:

$$T(\mathbf{x}, t) \sim \mathcal{GP}(\mu_{T_0}, K_{T_0}(t_i, t_j) + K_{T_1}(\mathbf{x}_i, t_i, \mathbf{x}_j, t_j) + K_{T^*}(\mathbf{x}_i, t_i, \mathbf{x}_j, t_j)) \quad (24)$$

This allows us to define a prior multivariate Gaussian distribution for \mathbf{T} , the vector of temperatures at all pairs $\{\mathbf{x}, t\}$ of space and time coordinates in X and τ :

$$\mathbf{T} \sim \mathcal{N}(\mu_{\mathbf{T}}, \mathbf{K}_{\mathbf{T}}) \quad (25)$$

where $\mu_{\mathbf{T}}$ is the mean vector and $\mathbf{K}_{\mathbf{T}}$ is the covariance matrix. Any observation \mathbf{y} of this temperature field can update this prior model to a posterior model as outlined in Section 2.2. Observations of the local temperature, e.g. as obtained from weather stations, are modeled as:

$$Y_T(\mathbf{x}, t) = T(\mathbf{x}, t) + \epsilon(\mathbf{x}, t) \quad \epsilon(\mathbf{x}, t) \sim \mathcal{GP}(\mathbf{0}, K_{\epsilon}(\mathbf{x}_i, t_i, \mathbf{x}_j, t_j)) \quad (26)$$

We assume a white-noise model for error $\epsilon(\mathbf{x}, t)$, with $M_{\epsilon}(\mathbf{x}, t) = 0$ and $K_{\epsilon}(\mathbf{x}_i, t_i, \mathbf{x}_j, t_j) = \delta_{ij} \sigma_{\epsilon}^2$, where δ_{ij} is the Kronecker delta.

Using this Gaussian process model for temperature, we can incorporate data from various sources for updating our temperature predictions and generating an improved posterior temperature model. Measurements of the forms of Eqs. (12), (18), or (26) can be expressed in the format of Eq. (6) through appropriate definition of $\beta_{\mathbf{y}}$. In this way, data from various sources, such as predictions from coarse resolution weather models, simulations of temperature patterns using fine resolution models, and field observations from weather stations, can be combined to update the prior temperature field model to a posterior model following Eqs. (8) and (9). Thus, the resulting temperature prediction accuracy can be improved.

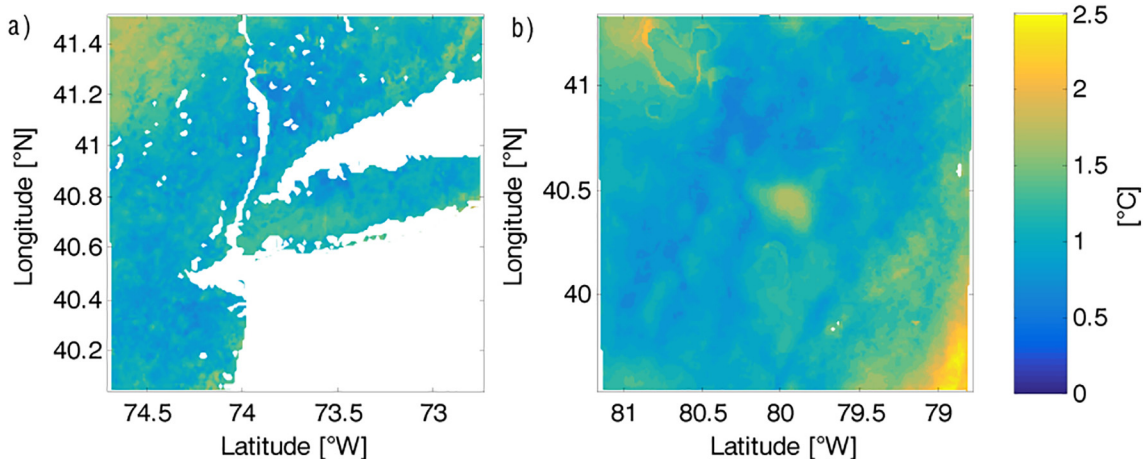


Fig. 7. Spatial standard deviation in the residual temperature field for the region of New York City, NY (a) and Pittsburgh, PA, USA (b).

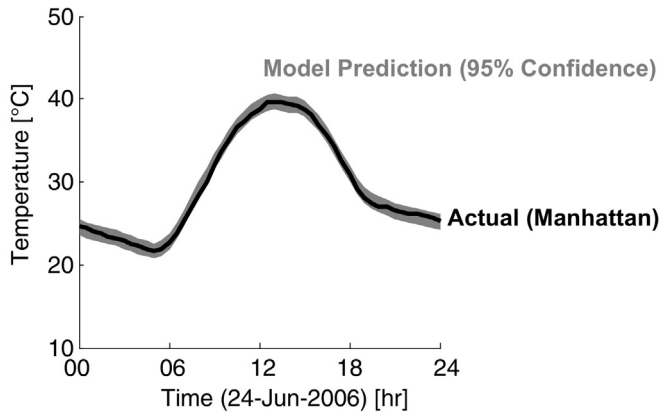


Fig. 8. Comparison of temperature records from WRF (black line) for a location on Manhattan Island with 95% confidence interval (grey area) of the posterior model for one-hour-ahead prediction under use Case 4.

3. Model calibration

The computational complexity of fine resolution physical models of urban microclimates generally precludes their use for short-term temperature forecasting. We instead make use of these models to train a spatio-temporal probabilistic model, which uses relatively fast probabilistic inference methods for temperature prediction. This section describes the generation of training data from a fine resolution model for New York City, NY and Pittsburgh, PA, USA and their use in calibrating the hyperparameters of the Gaussian process models discussed in Section 2. In this paper, we adopt a least-squares curve-fitting approach to match the empirical covariance derived from the training data to the parametric forms of the covariance functions. Furthermore, the hyperparameters of each component of the full Gaussian process model are trained separately, and these trained models are combined as discussed in Section 2.6. These steps are taken to reduce the

computational complexity of the calibration process with respect to typical maximum likelihood estimation techniques (Rasmussen & Williams, 2006).

3.1. Training data simulation using WRF-PUCM

To calibrate our probabilistic model, we use representative spatio-temporal temperature training data simulated from the WRF-ARW model (version 3.6) with the PUCM extension. The simulations use the North American Land-use Category Dataset (NLCD) 2006 to determine the land use and surface properties. Boundary conditions and initial conditions are obtained from the North American Regional Reanalysis data at 6 hr intervals. Three nested computational domains with horizontal grid resolutions of 9, 3, and 1 km are defined over the target city (New York City, NY, or Pittsburgh, PA, USA). This grid refinement uses only one-way coupling: larger domains provide boundary conditions to finer ones, but the smaller domains do not provide feedback. All domains use 60 vertical grid levels. Further information on the settings used for these simulations is provided in Appendix B.

The default urban canopy model (UCM) inside WRF is replaced by the PUCM (Wang et al., 2013), which also uses the energy exchange framework of Kusaka, Kikegawa, Kimura, & Kondo (2001). However, each facet (e.g. wall, roof, road) in the PUCM can be divided into sub-facets. The multiple sub-facets are modeled with distinct physical and thermal properties. PUCM also includes more realistic representations for hydrological processes, including in-canyon vegetated soils and water storage capacity for impervious materials. The PUCM coupled to WRF produces results which better capture the UHI compared to the default UCM (Li & Bou-Zeid, 2014), allowing the trained Gaussian process model to better reflect urban temperatures.

Apart from replacing the default UCM, the WRF simulations also use a mosaic-based approach (Li & Bou-Zeid, 2014) to compute the surface fluxes as opposed to the dominant category method commonly used in the default WRF-ARW. In the mosaic-based approach, instead of fixing a single land use category at each grid cell, the fluxes from up to 15 land

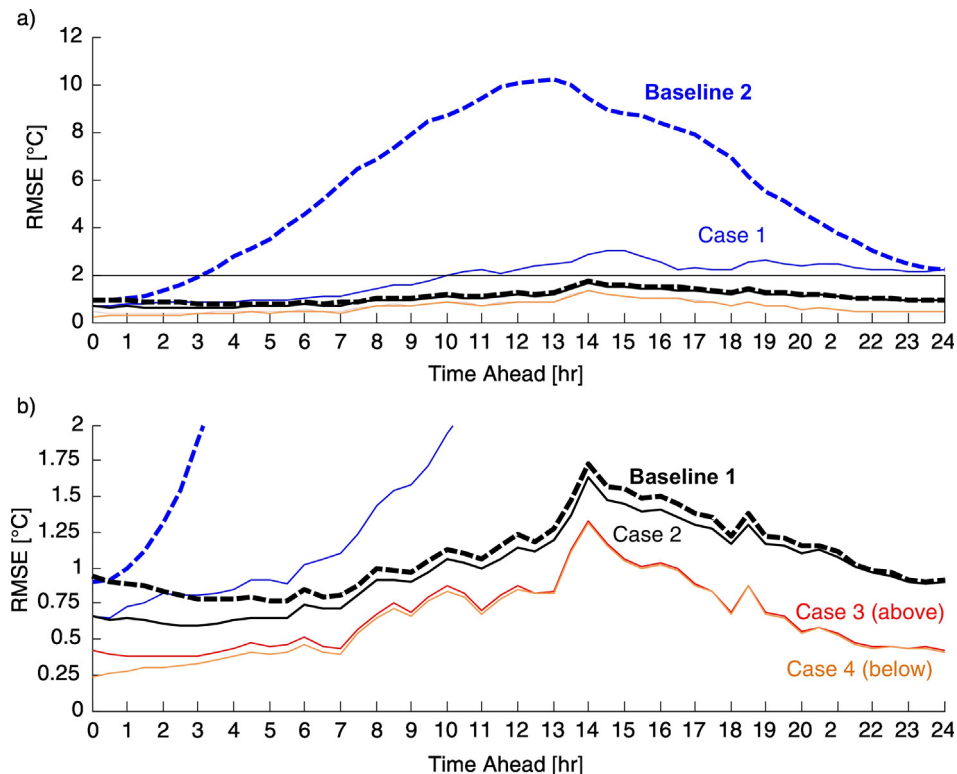


Fig. 9. Predictive performance of the probabilistic model for New York City, NY, under various use cases. For comparison, the performances of two baseline prediction cases are also provided. The boxed area of part (a) is depicted in more detail in part (b).

use types in that cell are solved and then fractionally summed to compute the fluxes into the atmosphere. This mosaic approach is more suitable for urban areas, where land uses vary on small length scales (Ramamurthy, Li, & Bou-Zeid, 2015).

Using this deterministic temperature model, we conduct a pair of simulations of summertime temperatures in both New York City and Pittsburgh. For each city, a shorter duration simulation provides data used to calibrate the Gaussian process model hyperparameters, and a longer one provides data for model validation (see Section 4). Table 1 summarizes the simulation settings.

Fig. 1 shows the land usage for the simulated regions around New York City and Pittsburgh for reference.

3.2. Global mean temperature

Fig. 2 compares the covariance model for the global mean temperature $T_0(t)$ from Eq. (11), calibrated from data simulated for New York City, and the observed temporal covariance pattern in the calibration data. Note the strong daily cyclic pattern.

Table 2 lists calibrated model hyperparameters. Note that μ_{T_0} represents the average temperatures for these cities from the training data, rather than the year-round average.

Fig. 3 presents an example of average temperature prediction for New York City. Note that the forecast confidence decreases as the prediction lead time increases. However, the daily periodicity of the temperature is preserved by the cyclic correlation structure.

3.3. Cyclic temperature pattern

Fig. 4 compares calibrated covariance functions for the cyclic temperature pattern in space from Eq. (15) and in time from Eq. (16) to the empirical covariance observed in simulated temperature data from New York City.

Note the negative empirical correlations in Fig. 4a. These are likely an artifact of the finite simulation domain used; if some areas of the domain are systematically above the global mean temperature, then others must necessarily be below this mean, leading to observed negative correlations. These are not included in the model, as the degree of negative correlation and the distance at which it occurs is dependent on the size of the simulation domain. Instead, it is assumed that the cyclic temperature patterns are independent as the distance between locations goes to infinity. To reduce the impact which the observed negative correlations have on model calibration, the simulation areas used to provide calibration data are larger than the areas over which the model is to be applied (as shown in Fig. 1).

Table 3 lists the calibrated hyperparameters. Note that, although both length-scale parameters are nearly the same for Pittsburgh, the model of Eq. (15) is still used for consistency.

Fig. 5 demonstrates the posterior mean field of the cyclic temperature pattern conditioned on measurements Y_{T_i} (as in Eq. (18)) for New York City at local midnight and noon. Note that the UHI effect for surface temperatures is more pronounced during the day than at night, as expected (Oke, 1997).

Table 6

Comparative results for New York City, listing RMSE for different models and prediction lead times.

Method	RMSE [°C] of lead time [hrs]			
	0	1	6	24
Case 1	0.66	0.72	1.02	2.17
Case 2	0.66	0.64	0.74	0.90
Case 3	0.42	0.38	0.51	0.42
Case 4	0.23	0.27	0.46	0.41
Baseline 1	0.94	0.89	0.84	0.91
Baseline 2	0.90	0.99	4.49	2.18

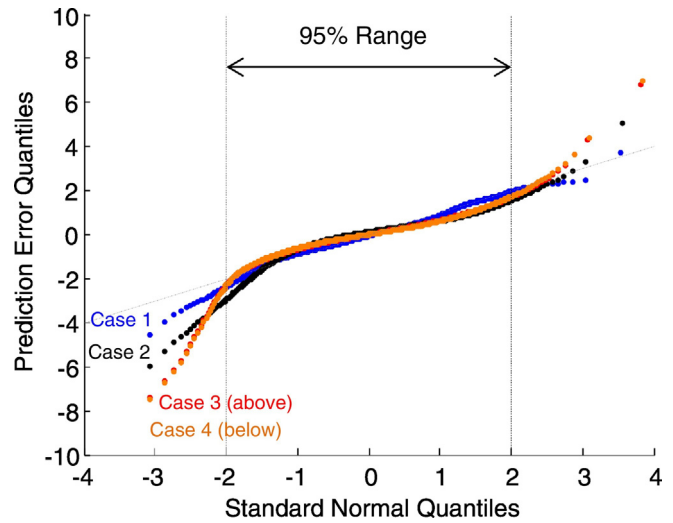


Fig. 10. Quantile-quantile plot of 1000 empirical residuals of the probabilistic model for New York City, NY, under each use case. The 95% confidence interval of the Gaussian distribution is indicated between the vertical dashed lines. The grey dashed line indicates the ideal normal distribution.

3.4. Residual temperature

Fig. 6 compares the empirical correlations of the residual temperature field for New York City and the fitted correlation models. As discussed for Fig. 4a, the observed negative correlation at long distance is likely due to the imposed balance between positive and negative residuals over the finite simulation domain. Table 4 lists the calibrated hyperparameters.

The standard deviation of the residual field is calibrated from the training data as:

$$\sigma_{T''}(\mathbf{x}) = \sqrt{\text{Var}_t[T(\mathbf{x}, t) - Y_{T_0}(t) - Y_{T_1}(\mathbf{x}, t)]} \quad (27)$$

where Var_t denotes the variance with respect to t . Fig. 7a shows the calibrated standard deviation field for New York City, and Fig. 7b shows this for Pittsburgh. In general, more mountainous areas appear to have higher variability.

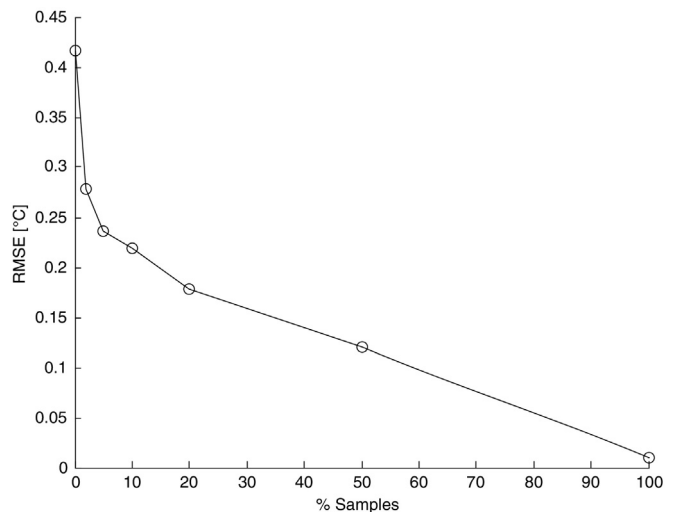


Fig. 11. Results for posterior model performance under use Case 4 with different levels of data (as measured by % Samples, or the fraction of locations at which data is collected for updating the model) for New York City, NY.

Table 7

Comparative results in Pittsburgh, listing RMSE in °C for different models and prediction lead times.

Method	RMSE [°C] of lead time [hrs]			
	0	1	6	24
Case 1	0.25	0.78	2.07	3.51
Case 2	0.38	0.73	1.29	1.12
Case 3	0.60	0.57	0.50	0.42
Case 4	0.27	0.43	0.51	0.42
Baseline 1	1.54	1.46	1.10	1.73
Baseline 2	0.27	1.39	6.71	3.41

4. Model validation

We assess the predictive performance of the Gaussian process model for temperature by assuming that the validation data simulated by WRF-PUCM represent the true surface temperature. We perform model testing under four representative use cases, as discussed below.

Case 1. Local temperature measurements $Y_T(\mathbf{x}, t)$, as in Eq. (26), are used to update the prior model. For this purpose, a random subset of grid points is selected to represent the locations of simulated weather stations. Validation data up to the current time at these locations constitute the measurement set Y , and from these data the posterior temperature prediction $\mathbf{T}|\mathbf{y}$ is obtained. A small error of $\sigma_e = 0.02^\circ\text{C}$ is assumed for these measures. Unless otherwise indicated, the simulated weather stations represent 5% of discrete locations, corresponding to an average density of one station per 20 km².

Case 2. In addition to the local measurements from Case 1, global average measurements $Y_{T_0}(t)$ with negligible error, as in Eq. (12), are available for past and future times. These global measures represent coarse resolution WRF model predictions from the NWS. Global average measures and local measurements constitute the measurement set Y from which $\mathbf{T}|\mathbf{y}$ is obtained.

Case 3. This case combines global average measurements as in Case 2 with measurements of the cyclic temperature patterns from the training period as observations $Y_T(\mathbf{x}, t)$ with negligible error, as in Eq. (18). This case illustrates combining prior runs of a fine resolution model with real-time runs of a coarse resolution model.

Case 4. This is the same as Case 3, but also includes the local measurements of Case 1.

Besides these use cases, we also consider two baseline cases which do not make use of the Gaussian process model:

Baseline 1. The global mean temperature $T_0(t)$ is used as an estimate of the temperature at each location. This represents the use of a coarse resolution weather forecast.

Baseline 2. Temperatures are predicted as the nearest weather station measurement (the same simulated stations described in Case 1 are used). That is, this baseline case has the same input as use Case 1, but does not use the Gaussian model to process this information.

Table 5 summarizes these cases and baselines according to what measures are included.

4.1. New York City, NY, USA

We conduct validation on a reduced domain of the full model, a 30 by 30 km area around Manhattan Island, in order to reduce the computational cost for updating the posterior model. We use 5 days of past local measurement data $Y_T(\mathbf{x}, t)$, one day of global average data $Y_{T_0}(t)$, and/or cyclic pattern measures $Y_T(\mathbf{x}, t)$ from the training data to condition the posterior model. This truncation of data records is an intuitive solution to reducing the computational cost of model updating, since more recent temperature measurements will “override” older measurements. For comparison, while the WRF-PUCM model takes about 12 h to generate one week of simulated temperatures, the calibrated probabilistic model can be run in 2 min (in Case 3) to 2 h (in Case 4) for the same period.

Fig. 8 compares a WRF-simulated (actual) temperature record at a location on Manhattan Island with the 95% confidence interval of the posterior model at that location under use Case 4. One-hour-ahead predictions are shown in this figure, with the nearest simulated weather station being 4 km away. This illustrates the probabilistic temperature estimates provided by the model.

To evaluate the predictive performance of the model, we use the calibrated prior model, together with temperature observations as per the use case, to obtain a posterior model for future temperatures during the validation period. The posterior mean of the model is used as the prediction. Accuracy is assessed using the average root mean square error (RMSE) between the predictions and the validation data, with the validation data divided into 10 subsets and the RMSE averaged across these subsets. Fig. 9 indicates the results of this assessment, and Table 6 summarizes the performance of the model for certain lead times.

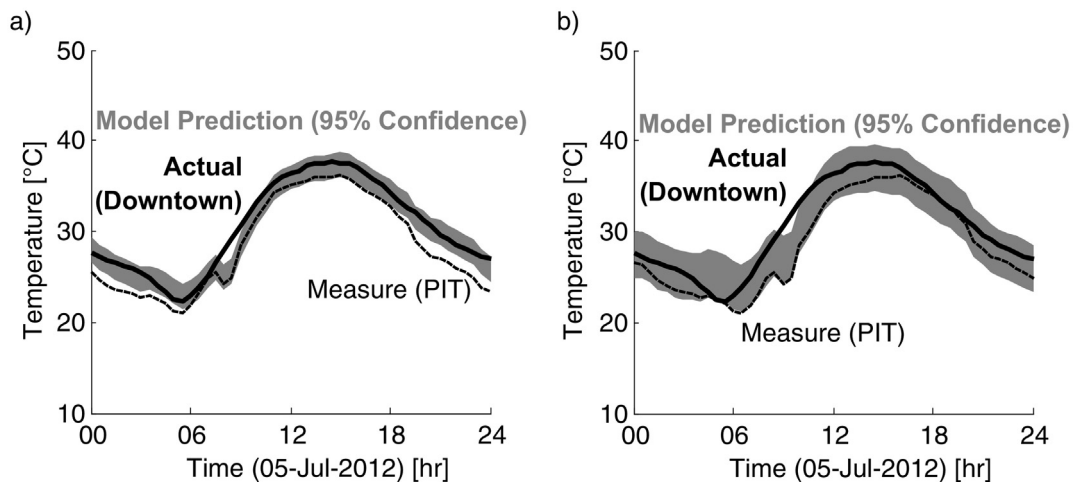


Fig. 12. Comparison of actual temperature in downtown Pittsburgh from the simulated temperature data of the validation period on the date indicated (solid line) with the measurement of the nearest weather station (dotted line) and the 95% confidence interval of the posterior prediction of the Gaussian process temperature model (grey area) for one-hour-ahead prediction under Case 4 with local data from the single weather station (a) and using this local measurement data as well as prior measures of the cyclic pattern obtained from the training data (b).

Predictive performance improves between use Cases 1, 2, 3, and 4, as more information is available. Performance for the base cases is comparable in the short-term. Performance of the second baseline is much poorer than other cases as the forecasting horizon increases since the most recent measures become increasingly out-of-date. The first use case, using the same input as the second baseline, performs fairly well in the short-term, but performance also declines with increasing forecasting horizon. Performance improves slightly at about 24 h lead time due to daily cyclic correlation. For Case 2, accurate forecasts of the global average temperature improve long-term performance, with this being comparable to the first baseline. The third and fourth cases, due to the inclusion of training data for spatial temperature patterns, outperform the first baseline, with the fourth case outperforming the third in the short-term due to local data.

For comparison, the RMSE of the WRF-PUCM model with respect to measurements at NWS stations has been approximated as 2 °C for near-surface air temperatures (Ramamurthy et al., 2015). The performance of the posterior model compares favorably with this value across all cases and lead times considered here. Since this probabilistic approach can be applied to other deterministic models and temperature data sets, improved simulation methods will allow future models to more accurately reflect true urban temperatures. For example, other recent improvements to the WRF urban canopy model, including better representations of urban foliage (Ryu, Bou-Zeid, Wang, & Smith, 2016) or anthropogenic heat and irrigation (Yang et al., 2015) might be incorporated, generating yet more accurate temperature simulations (Yang, Wang, Georgescu, Chen, & Tewari, 2016). Additionally, data from dense urban temperature monitoring networks, e.g. (Muller, Chapman, Grimmond, Young, & Cai, 2013), can be used for model calibration purposes.

The predictive performance of the model is also assessed from a probabilistic standpoint. A representative subset of the prediction errors discussed above is plotted in a quantile-quantile plot in Fig. 10, comparing their distribution against a Gaussian. This figure indicates that the errors have a nearly Gaussian distribution for about two standard deviations above and below the mean, covering the middle 95% of the data under all use cases. However, the true temperature field is non-Gaussian in the distribution tails. Fig. 10 indicates that the Gaussian model tends to over-predict positive errors and under-predict negative ones, i.e. the model predicts a wider distribution for temperatures than is actually observed. This phenomenon is more severe under use Cases 3 and 4 than under Cases 1 or 2. While this shortcoming might be addressed using a nonlinear transformation function between the model and the surface temperature, for the purposes of this paper, this approach is not adopted, and the resulting inaccuracies in predictions of extremes are taken as an acceptable source of error.

Finally, we vary the density of weather stations for use Case 4 and assess the impact on model performance. Fig. 11 reports the performance using various percentages (0%, 2%, 5%, 10%, 20%, 50%, 100%) of discrete locations as simulated weather stations. Note that the marginal benefit of adding stations is higher when the percentage is lower.

4.2. Pittsburgh, PA, USA

An evaluation of the performance of the calibrated model on the validation set is also conducted for Pittsburgh. Analysis is restricted to an area of 122 km² within the simulation region. Table 7 reports prediction accuracies, which are qualitatively similar to results for New York City. Interestingly, model performance in Case 1 for zero lead time slightly exceeds its performance in Case 4, which is comparable to the second baseline. This is likely due to the relatively small size of the region under consideration; measures at a small number of locations serve as an adequate representation of the temperature field. The utility of this model is clearer for greater lead times, as the performance of the model improves with increasing data for nonzero lead times and these

models show improved performance over comparable baseline cases, as previously noted for the example of New York City.

Finally, we demonstrate how this methodology accounts for the UHI by comparing temperatures from the validation data at a representative location in downtown Pittsburgh to the temperatures at the nearest NWS station at Pittsburgh International Airport (PIT), about 20 km distant. This is an example of the second baseline, with only a single measurement location. Alternatively, we process this data in the Gaussian process model according to use Case 4 (again with only the single local measurement at PIT) to obtain a posterior prediction for temperature at the downtown location. Fig. 12a compares one-hour-ahead predictions via both methods on a representative day during the validation period.

The downtown temperature tends to be higher than that measured at the airport due to the UHI. The measurements taken at PIT underestimate the downtown temperature by 1.5 °C on average, with a RMSE of 2.3 °C. By contrast, the posterior mean of the Gaussian process model only overestimates the downtown temperature by 0.1 °C on average during the validation period, with a RMSE of 0.7 °C. Thus, the Gaussian process model can account for systematic temperature differences due to the UHI using limited local measurement data, prior fine resolution simulation data, and accurate regional temperature forecasts.

We further perform a comparison without accurate regional temperature forecasts, as indicated in Fig. 12b. Note that this does not correspond to one of the cases listed in Table 5, but rather is a demonstrative case combining local measurement data $Y_T(\mathbf{x}, t)$ obtained at PIT with measures of the temperature pattern $Y_T(\mathbf{x}, t)$ from the training data. The PIT measures still underestimate downtown temperatures by 1.5 °C on average, with a RMSE of 2.3 °C, while the posterior model overestimates temperatures by 0.2 °C, with a RMSE of 1.6 °C. This demonstrates how, using only local measurement data and prior assessments of the UHI pattern, the model can account for systematic differences in temperature to reduce prediction bias with respect to the local measurement data alone.

5. Conclusions

This paper describes and demonstrates a method of combining fine resolution temperature simulation and probabilistic modeling for assessing surface temperatures in urban environments. Fine resolution modeling is necessary to capture the small-scale temperature differences in an urban environment due to the UHI. However, the computational demands of dynamic modeling preclude its real-time application to temperature prediction. Instead, using the results of such temperature simulations as training data, computationally efficient surrogate models are developed which allow for probabilistic prediction and updating based on gathered information. Similar models can be developed for other urban microclimate variables, e.g. near-surface air temperature or humidity.

One potential shortcoming of the probabilistic modeling approach outlined in this paper is the need for fine resolution training data for calibration. As shown in Section 3, hyperparameters can vary from region to region, and calibration should be performed for any new region to be modeled. Without proper calibration, data processing and posterior prediction may be inaccurate. Furthermore, appropriate characterization of measurement uncertainty is needed; if measurement accuracy is overestimated, posterior confidence intervals will be exaggerated. The robustness of this model to inaccurate hyperparameters is a subject for future investigation.

Besides temperature forecasting, this probabilistic model allows for pre-posterior analysis to optimize temperature measurement. This allows the utility of data in improving the predictive performance of the model to be assessed probabilistically. The companion paper (Malings et al., 2017) uses this model to perform such an analysis and determine optimal locations for temperature monitoring stations to best support

the updating of the prior probabilistic model under various metrics for sensor effectiveness.

Acknowledgements

This work was funded in part by the Metro21 Initiative project #3505715005755 at Carnegie Mellon University. Elie Bou-Zeid is funded by the Helen Shipley Hunt Fund of Princeton University and by US National Science Foundation's Sustainability Research Network Cooperative Agreement # 1444758. This work was also funded in part by the Dowd Fellowship from the College of Engineering at Carnegie Mellon University. The authors would like to thank Philip and Marsha Dowd for their financial support and encouragement. The authors would also like to thank S. Harris for contribution of the project title and acronym (SHADE).

Appendix A. Nomenclature

Table 8

Standard nomenclature used in the paper.

Term	Definition	Term	Definition
t	Time	τ	Temporal domain
\mathbf{x}	Spatial location or coordinate	X	Spatial domain
T	Surface temperature	F	Generic uncertain function
T_0	Global average temperature	α	Scaling hyperparameter
T_1	Cyclic temperature pattern	λ	Correlation length or timescale
T^r	Residual temperature	σ	Standard deviation hyperparameter
\mathbf{T}	Vector of temperature values	\mathbf{f}	Vector of function values
\mathbf{y}	Vector of measurements	\mathbf{Y}	Set of measurements, with subscript indicating the measured quantity
\mathcal{N}	Normal or Gaussian distribution	\mathcal{GP}	Gaussian process model
M	Mean function	$\boldsymbol{\mu}$	Mean vector
K	Covariance function	\mathbf{K}	Covariance matrix

Appendix B. Description of WRF-PUCM simulation settings

The WRF model used in this paper defaults to the following physical parameterization schemes: (i) the rapid radiative transfer model scheme for longwave radiation (Mlawer, Taubman, Brown, Iacono, & Clough, 1997); (ii) the Dudhia scheme (Dudhia, 1989) for shortwave radiation; (iii) the 2D Smagorinsky scheme for horizontal diffusion; (iv) the mosaic Noah land surface model for non-urban surfaces; and (v) the Mellor–Yamada–Janjic planetary boundary layer scheme (Mellor & Yamada, 1974) along with the modified Zilitinkevich relationship for thermal roughness length parameterization (Chen & Zhang, 2009). Cumulus parameterization schemes are not used in the simulations since they are not needed with the fine resolutions adopted here, as the convective scales are dynamically resolved.

References

Anderson, G. B., & Bell, M. L. (2011). Heat waves in the United States: Mortality risk during heat waves and effect modification by heat wave characteristics in 43 U.S. communities. *Environmental Health Perspectives*, 119(2), 210–218 (Feb.).

Andrews, K. (1994). *The consequences of heatwaves in Australia*. Hons. thesis. Sydney, Australia: School of Earth Sciences, Macquarie University.

NYCPCC (2013). *New York City panel on climate change (NYCPCC), climate risk information 2013: Observations, climate change projections, and maps, prepared for use by the City of New York special initiative on rebuilding and resiliency*. New York, New York.

Berko, J., Ingram, D. D., Saha, S., & Parker, J. D. (2014). *Deaths attributed to heat, cold, and other weather events in the United States, 2006–2010*. 76. Hyattsville, MD: National Center for Health Statistics.

Chen, F., & Zhang, Y. (2009). On the coupling strength between the land surface and the atmosphere: From viewpoint of surface exchange coefficients. *Geophysical Research Letters*, 36(10) (May).

Chen, X., -L., Zhao, H., -M., Li, P., -X., & Yin, Z., -Y. (2006). Remote sensing image-based analysis of the relationship between urban heat island and land use/cover changes. *Remote Sensing of Environment*, 104(2), 133–146 (Sep.).

Cressie, N. A. C., & Wikle, C. K. (2011). *Statistics for spatio-temporal data*. Hoboken, NJ: Wiley.

Davis, R., Knappenberg, P., Michaels, P., & Novicoff, W. (2003). Changing heat-related mortality in the United States. *Environmental Health Perspectives*, 111(14), 1712–1718.

Dewan, A., & Corner, R. (Eds.). (2014). *Impact of land use and land cover changes on urban land surface temperature* (pp. 219–238). Dhaka Megacity, Dordrecht: Springer Netherlands.

Dewan, A. M., & Yamaguchi, Y. (2009). Land use and land cover change in Greater Dhaka, Bangladesh: Using remote sensing to promote sustainable urbanization. *Applied Geography*, 29(3), 390–401 (Jul.).

Dudhia, J. (1989). Numerical study of convection observed during the winter monsoon experiment using a mesoscale two-dimensional model. *Journal of the Atmospheric Sciences*, 46(20), 3077–3107 (Oct.).

Geerts, & Linacre (1999). *Data from a newsletter of the Natural Hazards Research Centre*. Sydney, Australia: Macquarie University.

Homer, C. G., et al. (2015). Completion of the 2011 National Land Cover Database for the conterminous United States—Representing a decade of land cover change information. *Photogrammetric Engineering and Remote Sensing*, 81(5), 345–354.

Kalkstein, L. S., & Greene, J. S. (1997). An evaluation of climate/mortality relationships in large U.S. cities and the possible impacts of a climate change. *Environmental Health Perspectives*, 105(1), 84–93.

Krause, A., Singh, A., & Guestrin, C. (2008). Near-optimal sensor placements in Gaussian processes: Theory, efficient algorithms and empirical studies. *Journal of Machine Learning Research*, 9, 235–284.

Kusaka, H., Kikigawa, Y., Kimura, F., & Kondo, H. (2001). A simple single-layer urban canopy model for atmospheric models: Comparison with multi-layer and slab models. *Boundary-Layer Meteorology*, 101(3), 329–358 (Dec.).

Li, D., & Bou-Zeid, E. (2013). Synergistic interactions between urban heat islands and heat waves: The impact in cities is larger than the sum of its parts*. *Journal of Applied Meteorology and Climatology*, 52(9), 2051–2064 (Sep.).

Li, D., & Bou-Zeid, E. (2014). Quality and sensitivity of high-resolution numerical simulation of urban heat islands. *Environmental Research Letters*, 9(5), 055001 (May).

Li, D., Bou-Zeid, E., & Oppenheimer, M. (2014). The effectiveness of cool and green roofs as urban heat island mitigation strategies. *Environmental Research Letters*, 9(5), 055002 (May).

Li, W., Cao, Q., Lang, K., & Wu, J. (2017). Linking potential heat source and sink to urban heat island: Heterogeneous effects of landscape pattern on land surface temperature. *The Science of the Total Environment*, 586, 457–465 (May).

Lin-Jiong, Z., Yi-Min, L., Qing, B., Hai-Yang, Y., & Guo-Xiong, W. (2012). Computational performance of the high-resolution atmospheric model FAMIL. *Atmospheric and Oceanic Science Letters*, 5(5), 355–359 (Jan.).

Malings, C., & Pozzi, M. (2014). *Conditional entropy and value of information based metrics for sensor placement in infrastructure systems*. Proceedings of the 6th World Conference on Structural Control and Monitoring, Spain: Barcelona.

Malings, C., Pozzi, M., Klima, K., Bou-Zeid, E., Ramamurthy, P., & Bergés, M. (2017). *Surface heat assessment for developed environments: Optimizing urban temperature monitoring*. manuscript in preparation.

Melillo, J. M., Richmond, T. C., & Yohe, G. W. (2014). *Climate change impacts in the United States: The third national climate assessment*.

Mellor, G. L., & Yamada, T. (1974). A hierarchy of turbulence closure models for planetary boundary layers. *Journal of the Atmospheric Sciences*, 31(7), 1791–1806 (Oct.).

Menne, B., & Matthies, F. (2009). *EuroHEAT: Improving public health responses to extreme weather/heat-waves, technical summary*. World Health Organization.

Mlawer, E. J., Taubman, S. J., Brown, P. D., Iacono, M. J., & Clough, S. A. (1997). Radiative transfer for inhomogeneous atmospheres: RRTM, a validated correlated-k model for the longwave. *Journal of Geophysical Research-Atmospheres*, 102(D14), 16663–16682 (Jul.).

Muller, C. L., Chapman, L., Grimmond, C. S. B., Young, D. T., & Cai, X. (2013). Sensors and the city: A review of urban meteorological networks. *International Journal of Climatology*, 33(7), 1585–1600 (Jun.).

Mushore, T. D., Mutanga, O., Odindi, J., & Dube, T. (2017). Determining extreme heat vulnerability of Harare Metropolitan City using multispectral remote sensing and socio-economic data. *Journal of Spatial Science*, 62, 1–19.

Oke, T. R. (1997). Urban climates and global environmental change. *Applied climatology: Principles & practices* (pp. 273–287). New York, NY: Routledge.

Parson, M., & Jameson, J. (2012). *Pittsburgh climate action plan, version 2.0, Pittsburgh climate initiative*. Pittsburgh, PA: Green Building Alliance (Feb.).

Ramamurthy, P., Li, D., & Bou-Zeid, E. (2015). High-resolution simulation of heatwave events in New York City. *Theoretical and Applied Climatology* (Dec.).

Rasmussen, C. E., & Williams, C. K. I. (2006). *Gaussian processes for machine learning*. Cambridge, Mass: MIT Press.

Rhoades, E. K., Contreras, C., Garrett, S. K., Bakshi, M., & Bellomo, A. J. (2014). *Your health and climate change in Los Angeles County*. Los Angeles County Department of Public Health. 1. (Aug.).

Robine, J., -M., et al. (2008). Death toll exceeded 70,000 in Europe during the summer of 2003. *Comptes Rendus Biologies*, 331(2), 171–178 (Feb.).

Ryu, Y., -H., Bou-Zeid, E., Wang, Z., -H., & Smith, J. A. (2016). Realistic representation of trees in an urban canopy model. *Boundary-Layer Meteorology*, 159(2), 193–220 (May).

Sailor, D. J. (2002). *Urban heat islands, opportunities and challenges for mitigation and adaptation, presented at the North American Urban Heat Island Summit*. Toronto: Ontario, Canada.

Skamarock, W. C., et al. (2005). *A description of the advanced research WRF version 2, National Center for Atmospheric Research, NCAR/TN-468 + STR*. (Jun.).

Sper de Almeida, E., & Bauer, M. (2012). Reducing time delays in computing numerical weather models at regional and local levels: A grid-based approach. *International Journal of Grid Computing & Applications*, 3(4), 1–17 (Dec.).

- Straub, D. (2011). Reliability updating with inspection and monitoring data in deteriorating reinforced concrete slabs. *Proceedings of ICASP11*.
- Sustainable, D. C. (2013). *Sustainable DC Plan*. Washington DC.
- Trotter, L., Dewan, A., & Robinson, T. (2017). Effects of rapid urbanisation on the urban thermal environment between 1990 and 2011 in Dhaka Megacity, Bangladesh. *AIMS Environmental Science*, 4(1), 145–167.
- US EPA (2012). *Reducing urban heat island: Compendium of strategies — Urban Heat Island basics*. Washington, DC, USA: U.S. Environmental Protection Agency.
- Wang, Z. -H., Bou-Zeid, E., & Smith, J. A. (2013). A coupled energy transport and hydrological model for urban canopies evaluated using a wireless sensor network. *Quarterly Journal of the Royal Meteorological Society*, 139(675), 1643–1657 (Jul.).
- Worley, P. H., Mirin, A. A., Craig, A. P., Taylor, M. A., Dennis, J. M., & Vertenstein, M. (2011). *Performance of the community earth system model*, 1.
- Yang, J., Wang, Z. -H., Georgescu, M., Chen, F., & Tewari, M. (2016). Assessing the impact of enhanced hydrological processes on urban hydrometeorology with application to two cities in contrasting climates. *Journal of Hydrometeorology*, 17(4), 1031–1047 (Apr.).
- Yang, J., et al. (2015). Enhancing hydrologic modelling in the coupled weather research and forecasting — Urban modelling system. *Boundary-Layer Meteorology*, 155(1), 87–109 (Apr.).